Direct Spot Joining of Thin Gauge Aluminum Alloy to Stainless Steel and Joint Performance in A Corrosion Environment

Abdul Sayeed Khan¹, Pingsha Dong^{1,2,*}, Kai Sun³, Doug Larsen⁴

Affiliations:

¹Department of Naval Architecture and Marine Engineering, University of Michigan, Ann Arbor, MI 48109, USA

²Department of Mechanical Engineering, University of Michigan, Ann Arbor, MI 48109, USA

³Department of Materials Science and Engineering, University of Michigan, Ann Arbor, MI 48109, USA

⁴Advanced Engineering Sealing, Cooper Standard, Livonia, MI 48150, USA

*Corresponding authors. Email: dongp@umich.edu (P. Dong),

Abstract

Direct joining of aluminum alloy and steel sheets offers a great potential for achieving effective structural lightweighting for transportation systems. The major challenge is how to avoid the formation of brittle intermetallic compounds (IMCs), which can be detrimental to joint load capacity and corrosion resistance. This paper presents a friction-based direct solid-state joining method for welding thin aluminum alloy (AA6061-T6) to stainless steel (316). Using a flat head friction stir tool, a strongly bonded interface was achieved under a steady-state dwell time of 20-sec and 1000 rpm by avoiding excessive heating via keeping the friction tool pin away from the steel surface, eliminating introducing detrimental IMCs. The effects of an automotive-relevant corrosion environment condition on joint strengths are considered. Mechanical test results show that aluminum and stainless-steel spot joints produced by the proposed method exhibit no corrosion-induced damage or cracking nor any noticeable reduction in strengths, resulting in dominantly ductile failure mode.

Keywords: Dissimilar material joining, solid state welding, shear localization, intermetallic compounds (IMCs), corrosion, joint strength.

1. Introduction

A multi-material approach to achieve effective structural lightweighting has gained increasing attention over the last decade [1–3]. As such, effectively combining steel with aluminum alloy can be a cost-effective means of attaining high strength-to-weight ratios in transportation systems, particularly for mass-produced automotive structures [4]. Another promising area of the multi-material applications approach is non-structural. These include thin gauge aluminum and steel combinations for automotive interior and exterior trims, weathering strips, and other related components [5–7]. Due to the nature of the high-volume production of these products, cost-effective dissimilar material joining methods become essential for realizing the potential of multi-material systems. This becomes particularly challenging when dealing with metallurgically incompatible material combinations, e.g., by directly welding an aluminum alloy to a steel substrate [8] (or polymer composite to metal [9–13]).

It is well known that fusion-based welding methods introduce brittle intermetallic compounds (IMCs) at the aluminum alloy and steel (Al/Steel in short) interface [14,15]. The presence of a certain amount of IMCs can cause cracking during welding and degrade joint load capacity for structural applications [16]. In addition, IMCs have been shown to be highly susceptible to galvanic corrosion under service environments [17].

As a result, solid-state joining methods have been considered in the research community. These include friction welding [18] and friction stir welding [19,20], roll bonding [21], magnetic pulse welding [22], and vaporizing foil actuator welding (VFAW) [23,24] for joining the two incompatible metals directly. The first two methods have shown their potential, but consistently mitigating detrimental IMCs remains to be the major challenge. The last two are mostly investigated for some special applications, and VFAW uses a controlled high velocity impact to

showed that heat input during the friction joining of the aluminum alloy and the steel significantly affected the joint strength as a result of IMCs. The heat input during the joining process is further correlated with the IMC layer thickness, and the joint strength is significantly affected by the thickness of the IMCs at the interface. The joint strength was found to show a significant improvement with a reduction in IMC thickness. Kimapong et al. [26] reported that an IMC thickness of $\sim 7~\mu m$ reduced the joint strength by $\sim 60\%$ for a joint compared to its strength when an IMC thickness was $\sim 1~\mu m$. Tanaka et al. [27] reported that the joint strength can be affected as much as three times when IMC thickness is reduced from $\sim 1~\mu m$ to $\sim 0.1~\mu m$. Watanabe et al. [28] showed that the thickness of the IMC layer in aluminum to steel joint under FSW increased with spot welding time used. There have been attempts of an intermediate transition layer, such as using Zn-based filler material [29] and utilizing the effect of silicon on Al-Si-based filler materials [30]. However, the presence of IMCs still cannot be avoided.

It is well established that aluminum to steel joints are prone to galvanic corrosion, which can be further adversely affected by the presence of IMCs [17]. Wloka et al. [29] demonstrated that the cathodic material (Fe) containing IMCs increases the dissolution of base material under a corrosive environment significantly. Shi et al. [31] showed that IMCs help formulate the galvanic cell at the interface and dissolve the base metals, accelerating the corrosion process further. Sravanthi et al. [32] have shown that the IMCs participate in galvanic corrosion and can further accelerate the corrosion process with increased layer thickness. Ma et al. [33] have shown that the corrosion potential is severely affected if the IMC layer thickness is high and the corrosion resistance drops. Reducing the IMC layer thickness to the sub-micron level is, hence, critical for achieving structurally applicable and corrosion-resistant joints between aluminum and steel. The

corrosion behavior of these dissimilar material joints thus is a defining factor for a successful structural application.

Several efforts have been used to either reduce the IMC layer thickness via controlling the heat input during the joining process or eliminate any IMCs at Al/Fe interface, including the stationary shoulder and buttering technique [25,34–36]. Along this line, noteworthy recent studies by Liu et al. [37] have shown that two dissimilar materials, e.g., aluminum alloy (AA6061-T6) and stainless steel 304, can be successfully joined together using a novel friction stir additive manufacturing (FSAM) method without detrimental IMCs at the interface through a controlled nanoscale shear localization induced amorphization (NSSLIA) process. Liu et al. [37] utilized a flat shoulder friction stir tool with a flat head pin and maintained a certain distance above the steel faying surface after penetrating the tool into the overlapped aluminum sheet. The rotating tool was then moved along the overlap length, maintaining the gap above the steel faying surface, enabling the NSSLIA process. Zhang et al. [38] further proved that the amorphous layer formed between the Al/Steel binary joints is stable and does not degrade or thicken under high-temperature post-heat treatment.

Encouraged by the recently discovered NSSLIA process for thick sheet aluminum alloy and steel combinations, this study is focused on achieving direct spot-joining of thin gauge aluminum alloy to stainless steel sheet by suppressing the IMCs at the interface by the NSSLIA process, develop a continuous amorphous reaction zone compared to discontinuous amorphous layer achieved for thick metallic sheet pairs and significantly improve the corrosion resistance. After establishing bond quality and probable presence of amorphous phase at the bonding interface, the effects of a well-adopted automotive corrosion cycle on the resulting weld nugget

morphology and spot joint strengths are then investigated in detail to explore the applicability of thin sheet spot joints for automotive applications under severe environmental conditions.

Table 1: Chemical compositions of stainless steel 316 (wt%).

	Fe	Cr	Ni	Mo	Mn	Cu	С	Si	N	S	P	Ti
SS316	Bal.	16-18.5	10-15	0-3	0-2	0-1	0-0.08	0-1	0-0.1	0.35	0-0.045	0.7 max

Table 2: Chemical compositions of AA6061-T6 alloy (wt%).

	Al	Mg	Si	Fe	Cr	Cu	Zn	Mn	Ni	Ti	Other
AA6061	Bal.	1.1	0.73	≤0.7	0.08	0.29	≤0.25	≤0.15	≤0.05	≤0.15	0.15

2. Materials and methods

Aluminum 6061-T6 alloy sheets of 0.60 mm in thickness and SS316 stainless steel sheets of 0.76 mm in thickness were chosen to be joined for consideration in an automotive component. The chemical compositions of SS316 and AA6061-T6 are provided in Table 1 and

Table 2, respectively, and their mechanical properties are listed in Table 3. A friction spot joining process was designed for this study by adopting a recently developed nanoscale shear localization process [37], as illustrated in Figure 1. The novelty of the shear localization-induced solid-state joining between the aluminum alloy and steel lies in the fact that it is capable of eliminating or minimizing the generation of IMCs. The process implemented here employs a nonconsumable flat head tool with a shoulder and pin, as depicted in Figure 1. The pin used has a diameter of 8 mm and is maintained at a constant height "h" above the aluminum alloy/steel (Al/Fe) interface, as discussed in [37]. For the present study, it was set as $\frac{h}{t} = \frac{1}{3}$, where t refers to the thickness of aluminum sheet and maintained throughout the process. The steel surfaces were received with #8 mirror polished surface condition securely covered with an adhesive back

polymer film to avoid any contamination, and no surface or bulk material treatment was performed on aluminum alloy sheets. However, both sheets were cleaned using ethanol to remove dirt and grease from the surfaces. Although the perfectly flat steel faying surface without microscopic scratches is the primary requirement for this joining process, a mirror-polished surface was a final product surface requirement.

Table 3: Mechanical properties of base metals

	Yield Strength (MPa)	Ultimate Tensile Strength (MPa)	Elongation (%)
AA6061 <mark>-T6</mark>	276	310	12
SS316	290	580	50

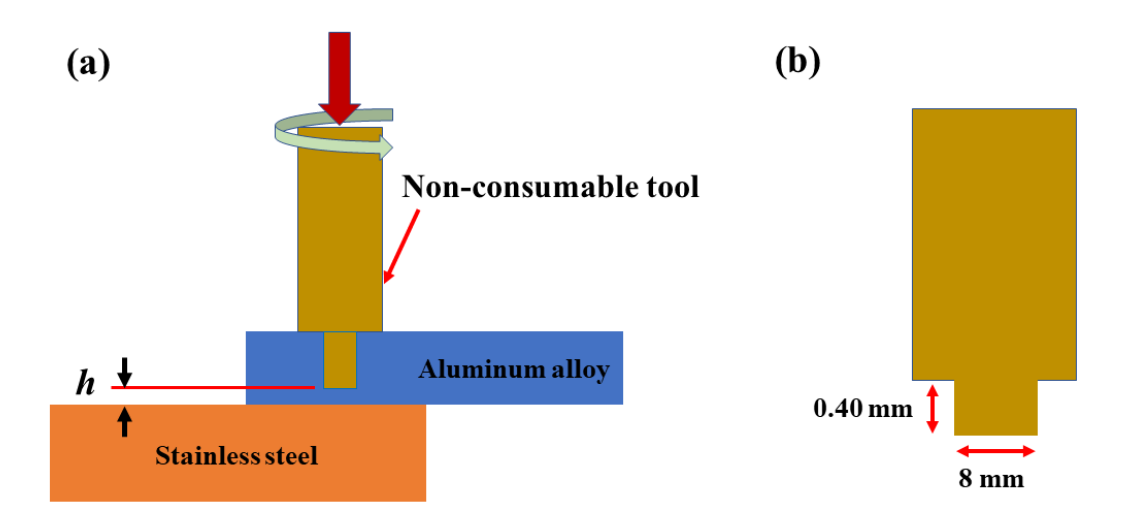


Figure 1: Friction spot joining process schematic: (a) tool placement with respect to the aluminum and steel sheets, and (b) critical dimensions of the friction stir tool

The steel sheet was treated as the substrate, and the aluminum alloy sheet was placed on the top in the spot joining configuration, as shown in Figure 1. During the process, the non-consumable tool rotation speed was set at 1000 rpm under displacement control mode for 20 seconds. For process characterization purpose, temperature measurements on a number of selected

samples were made by placing probe K-type thermocouple near the joint interface under the tool footprint, as illustrated in Figure 2a. A typical temperature history measured is shown in Figure 2b.

For comparing with and without corrosion effects on joint strengths, one batch of the spot joined specimens was subjected to GMW 14872 automotive-grade corrosion (Cycle C), under which this batch of the samples underwent 18 repeated corrosion cycles. Each cycle consisted of an ambient stage at 25 °C for 8 hours, humidity exposure at 100 % relative humidity at 49 °C for another 8 hours, and then a water fog chamber with 30% relative humidity at 60 °C for the 8 hours as well. The salt mist solution consisted of 0.90 wt% NaCl, 0.10 wt% CaCl₂, and 0.075 wt% NaHCO₃ in deionized water.

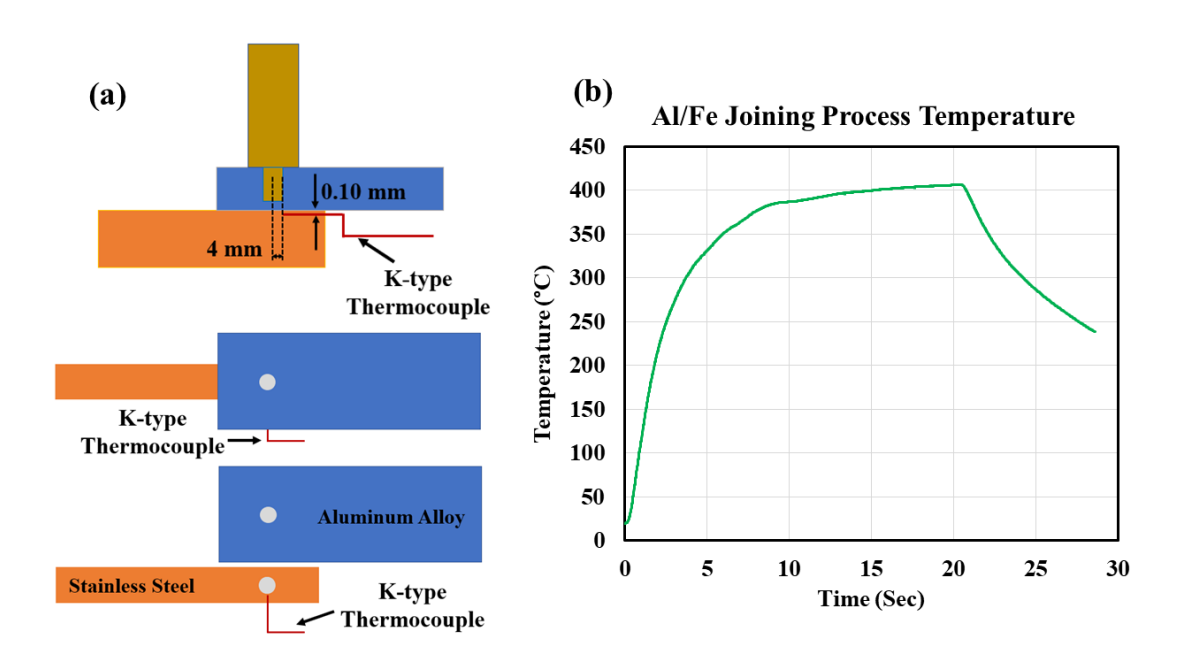


Figure 2: Joining process temperature measurements, (a) thermocouple placement schematic, and (b) temperature profile

Weld cross-section analyses were performed on both with and without being subjected to the aforementioned corrosion cycles by using a Nikon optical microscope and TESCAN MIRA 3 FEG scanning electron microscope (SEM). Cross sections across the weld nugget were removed using a wire electric discharge machine (EDM). Samples were ground using silicon carbide grit papers up to P800 size and then were polished up to 1 micron using the diamond polishing solution for further cross-section examinations. Both secondary electron images and backscattered electron images were collected at 5kV-15kV voltage and 15kV voltage, respectively. In-situ focused ion beam (FIB) liftouts for transmission electron microscopy (TEM) analysis across the Al/Steel bonding interface were prepared using a Thermo-Fisher (TFS) Nova 200 Nanolab FIB/SEM system. A TFS Spectra 300 Probe-Corrected S/TEM with two 60mm² SDD detectors attached was used for both imaging and spectroscopy using X-ray signals operated at 300kV in STEM mode.

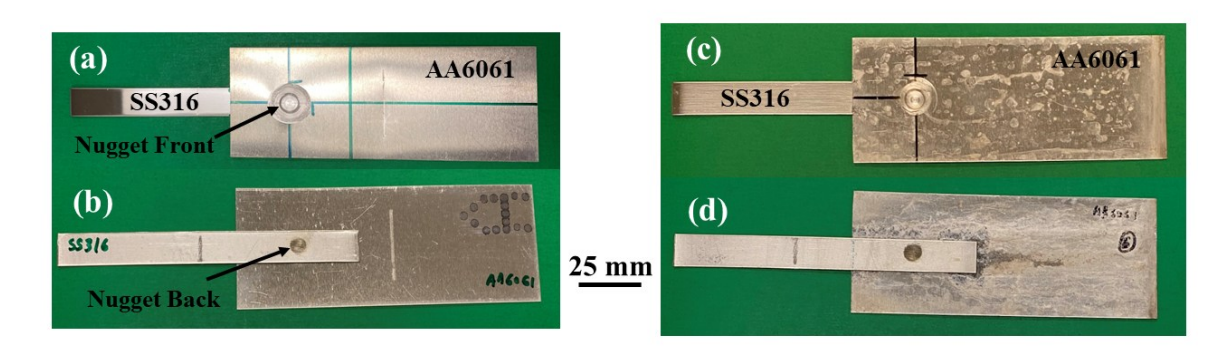


Figure 3: Al/Fe joints: (a) & (b) before the corrosion cycle, front and back sides of the sample, respectively, and (c) & (d) post-corrosion cycle, front and back sides of the sample, respectively.

The Al/Fe joint samples before and after subjecting to corrosion cycles are shown in Figure 3. Due to the lack of any specific testing standard for directly joined bi-metallic spot joint samples of thin sections, non-standard sample dimensions and testing configurations were adopted in this study to best accommodate the finished product requirements after joining. Three specimens corresponding without and three with corrosion effects were mechanically tested under lap shear tension conditions. A loading rate of 1 mm/min was used to be consistent with the quasi-static loading definition in an Instron 3382 load frame with a 100 kN load cell. To eliminate the global eccentricity with respect to the applied load line generated due to the unequal thickness and lap

configuration, rectangular tabs of complementing thicknesses were placed at the gripping locations of the joints during the lap shear tensile experiments, as can be seen in Figure 4. The load capacity of the test specimens or peak load reached prior to final failure (i.e., separation) of the joints under quasi-static loading conditions are summarized in Figure 9.

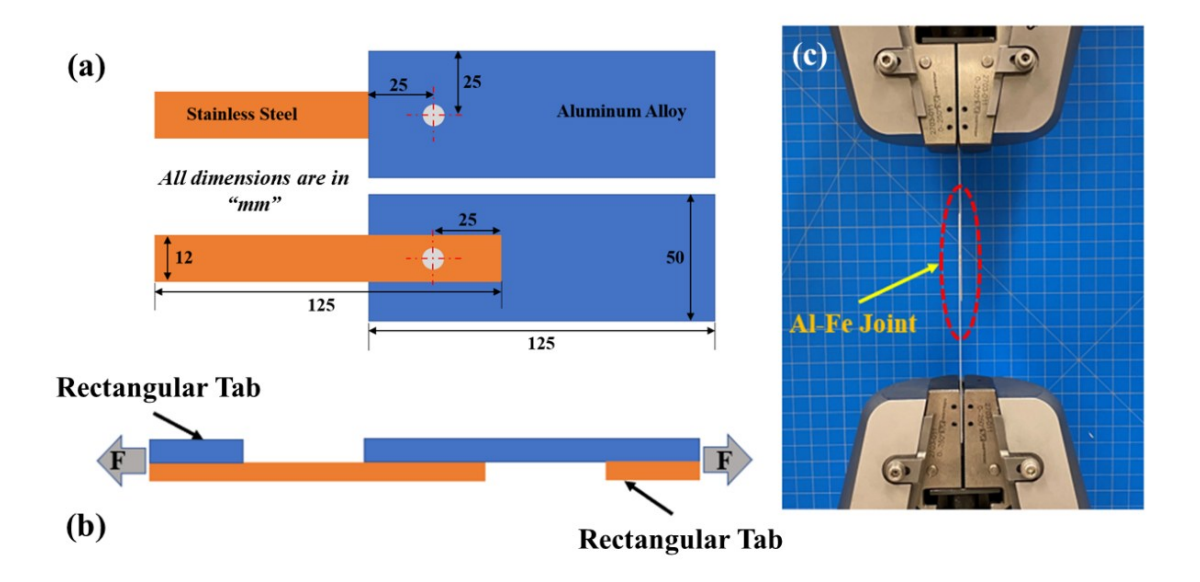


Figure 4: Lap shear tensile experimental schematic, (a) & (b) sample dimensions and shims/tab placement, (c) experimental setup with Al/Fe joint sample

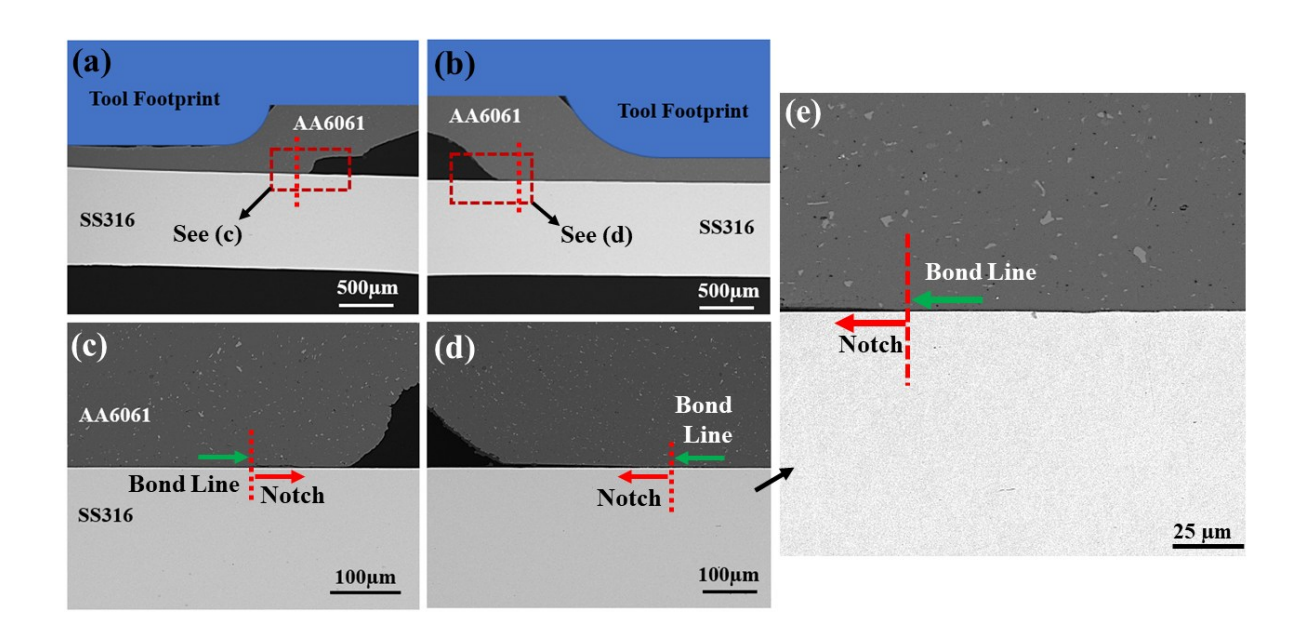


Figure 5: Cross-sectional SEM images of Al/Fe joint nugget shoulder, (a) before corrosion cycles; (b) after corrosion cycles; (c) high resolution detailed view from (a); (d) high resolution detailed view (b); and (e) high resolution detailed view near the notch from (d)

3. Results

3.1 Al/Fe interfacial bond formation characteristics

As described above, a constant value of $\frac{h}{t} = \frac{1}{3}$ was set to generate frictional heating and material flow just above the steel sheet surface to induce shear localization bonding [37] at the aluminum/steel interface. As shown in Figure 2B, the measured temperature follows a continuously increasing profile after the initial transient nonlinear part up to 10 seconds of joining process time. Figure 2b shows that the maximum temperature during the spot joining process reaches 406°C, which is well below the solidus to liquidus phase transition temperature (652 °C) of AA6061-T6 [39]. As shown in Figure 3, the samples indicate a spot joint formation by looking both from the front and back sides (see Figures 3a and 3b). There seems to be no significant change in sample surface appearances after being subjected to the corrosion cycles, particularly around the weld nugget regions (see Figure 3c and 3d).

To examine the local effects of corrosion environment exposure on weld nugget region,

Figure 5 shows macro- and microscopic examinations of one side of the spot joint in different magnification scales. The green arrow lines show that the Al/Fe bonding line ends (i.e., where the interfacial notch begins) slightly beyond the tool footprint edge. Again, there appear to be no significant differences between without and with being subjected to the corrosion cycles by comparing

Figure 5a and 5c with

Figure 5b and 5d. One subtle change in appearance as a result of the corrosion environment can be seen by comparing

Figure 5c and 5d at a $100 \mu m$ magnification scale. A light opening of the interfacial notch becomes more obvious in

Figure 5d after corrosion cycling than that without going through corrosion cycling. This could be attributed to temperature cycling associated with corrosion cycles described earlier. There is no sign of stress corrosion cracking into the weld nugget from the interfacial notch tip, as shown in

Figure 5e under an even higher magnification. This was further confirmed by the intimately bonded Al/Fe interface away from the shoulder locations shown in Figure 6 (a-d) at higher magnifications SEM images and also by the nugget profile on the post-corrosion sample shown in Figure 10d, suggesting that the joining interface at and around the joining nugget is intimately bonded under the tool footprint.

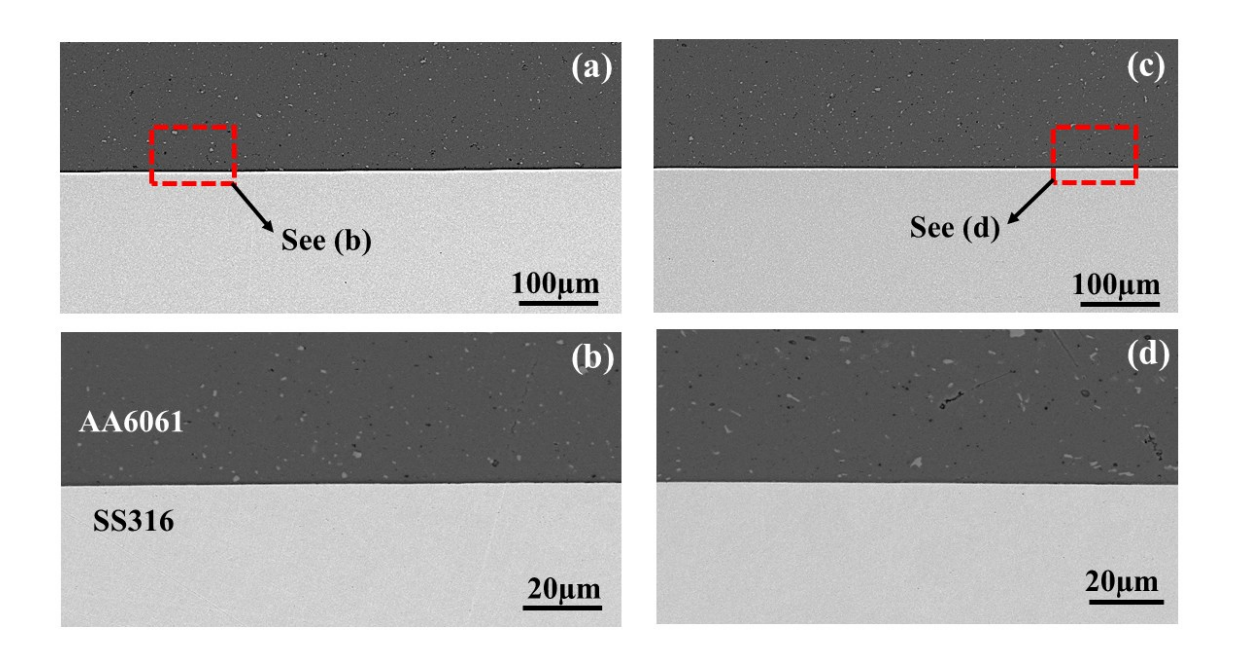


Figure 6: Cross-sectional SEM micrographs at the nugget center of Al/Fe joints, (a) & (b) low resolution images before corrosion cycles, and (c) & (d) high resolution images after corrosion cycles

Figure 6 shows the Al/Fe cross-section images obtained from SEM at the center of the nugget for both before and after the corrosion cycles. Both before and after the corrosion cycles cases show a significantly flat interface without scratches or mechanical irregularities. It can be observed from Figure 6 that the Al/Fe interfaces don't have any cavities or visible voids. It should be noted here that the steel surface used here was industrially mirror-polished and must be

significantly flat. Higher resolution images from SEM shown in Figures 6b and 6d don't show signs of IMCs, implying that the Al/Fe interface is strongly and intimately bonded without noticeable IMCs at the micron length scale. The absence of IMCs at this length scale for the post-corrosion sample, as shown in Figure 6d, also confirms that the corrosion cycle didn't induce any IMCs at the Al/Fe bonding interface.

3.2 Interface chemical composition and nanoscale structure

Figure 7 shows an HAADF image and its corresponding STEM BF images. There is no irregularity or discontinuity at the Al/Fe interface through-out the bonding length. Both magnified BF and HAADF images clearly depict an interface without any IMCs up to a 25 nm length scale (see Figure 7e and 7f). BF image shows a contrastingly darker area in Figure 7b, and corresponding brighter areas are marked with red arrows in the HAADF image, as shown in Figure 7a. These areas can be seen more clearly in Figures 7d and 7c, respectively, at a higher magnification. These brighter areas are adjacent to the Al/Fe interface and are on the steel material. Since the end surface of the tool-tip is placed away from the steel surface, the steel material does not experience a direct friction stirring effect. However, the bright areas forming an irregularly shaped band in the HAADF image shown in Figures 7a, 7c, and 7d imply partial crystal distortion induced by the formation of a phase band in the regions. The bright-band regions are up to an average length of 200 nm from the Al/Fe interface due to an indirect effect of high strain rate shear deformation occurring in the aluminum material side under the tool-tip surface.

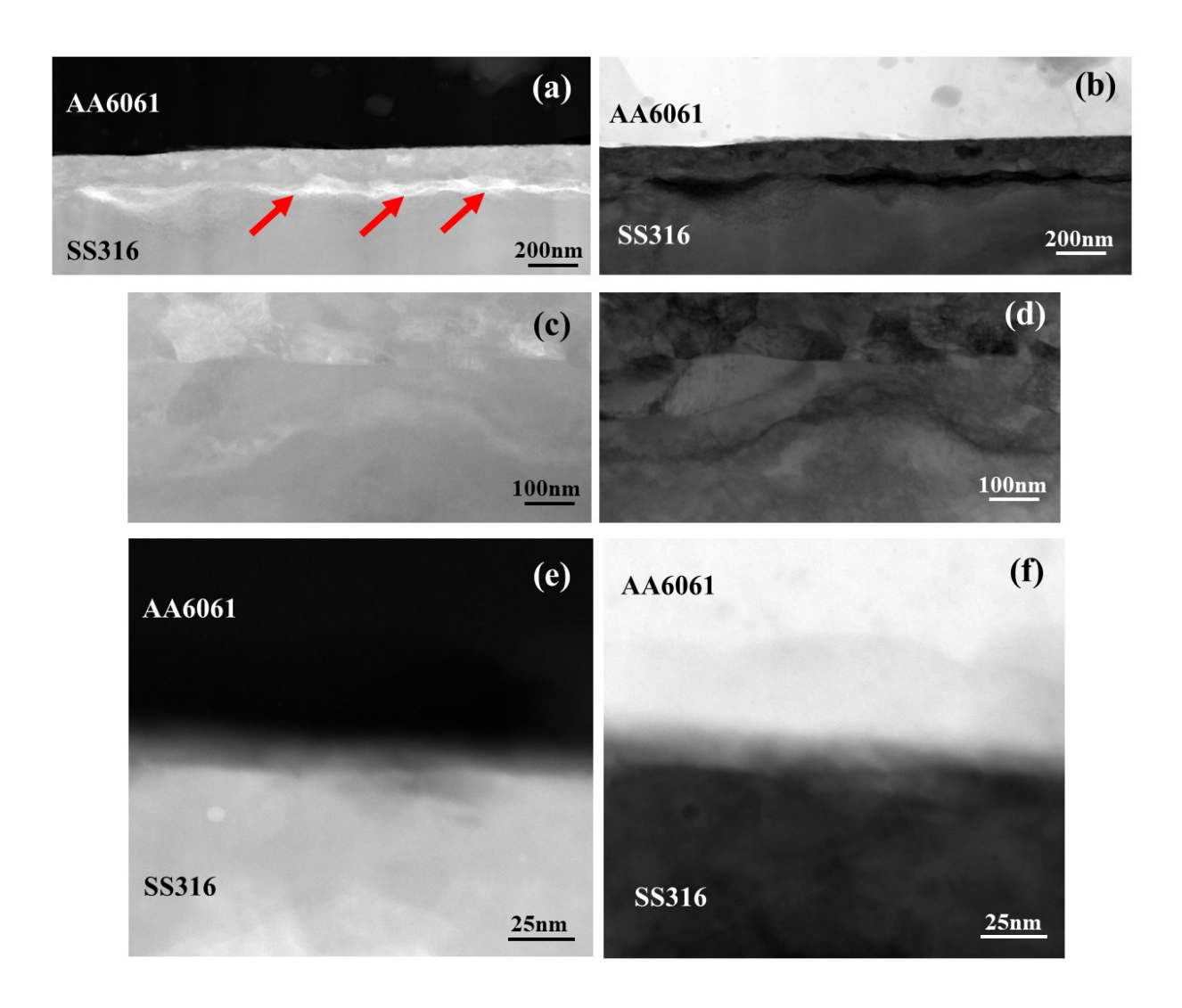


Figure 7: High-resolution cross-sectional STEM images of the Al/Fe joints at the nugget center, (a) (c) & (b) high-angle annular dark field (HAADF) images, and (b) (d) & (f) bright-field images, (c) and (d) showing the high-magnification images near the red arrows marked in (a).

Figure 8 shows corresponding elemental maps obtained from the area shown in HAADF images in Figure 7a. The elemental maps further elucidate that aluminum is fully intact above the bonding interface and iron is restricted below the bonding interface. Major alloying elements Mg and Si are spread in a thin layer with an order of 40-50 nm throughout the bonding interface, as shown in Figure 8. There is also a very thin layer of O distribution throughout the bonding

interface, as shown in Figure 8. This can be attributed to the native aluminum oxide on the surface, which is usually in the range of ~ 10 nm on the surface before joining occurs [37]. A noteworthy observation can be made from Figure 8 and Figure 13 that none of these significant alloying elements is cross-distributed in more than 50 nm length across the interface and are found to be contained in very narrow proximity from the Al/Fe interface or the bond line.

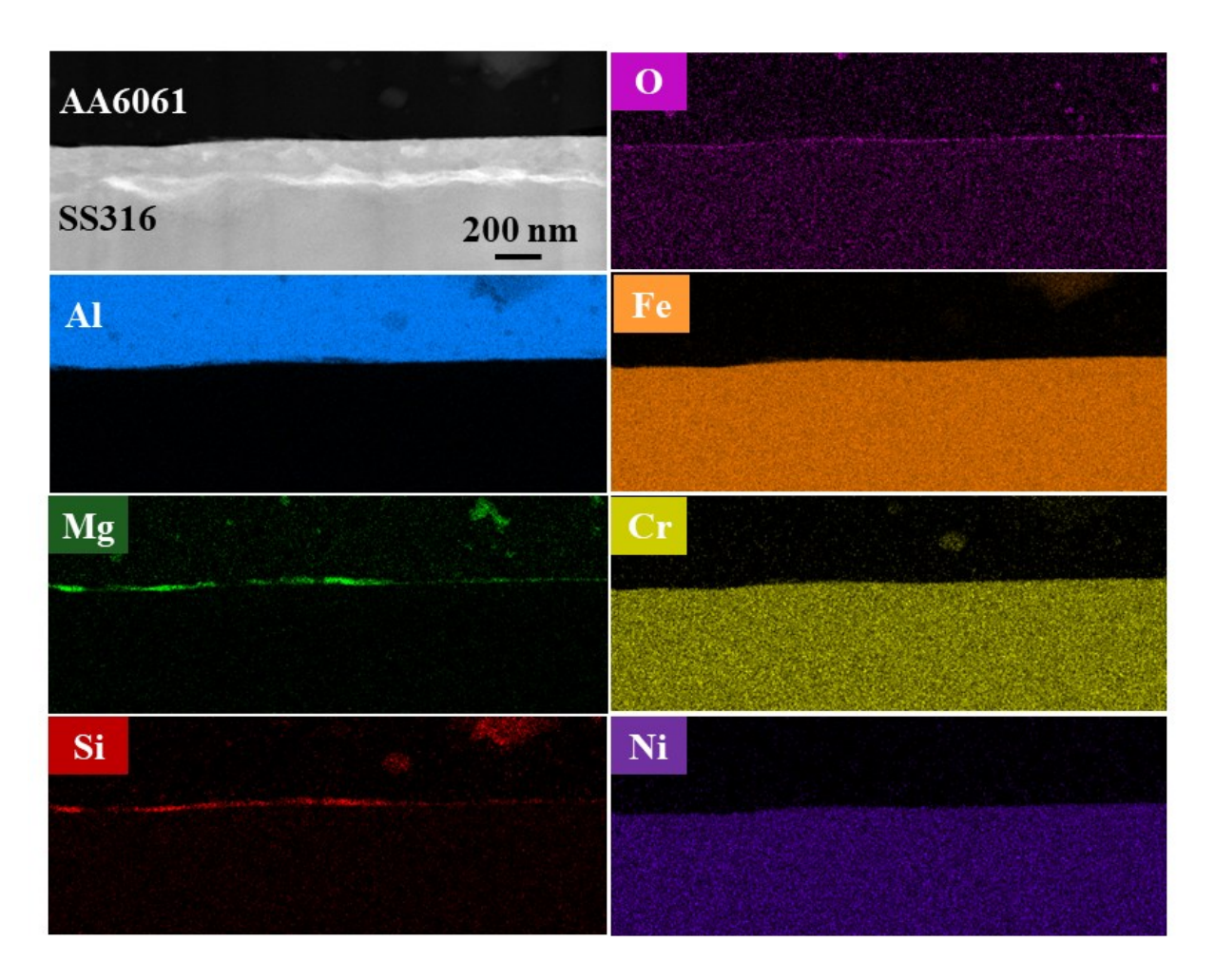


Figure 8: STEM HAADF image at the nugget center cross-section of the Al/Fe joint and EDS elemental maps

The red dashed boundaries shown in Figure 13b further depict the alloying elements' reactions or inter-diffusion. This reaction zone's thickness was measured to be around 45 nm. A closer look at the reaction zone provided a noteworthy observation of the presence of Mg and O elements, including Cr and Si, in considerable amounts. As shown in Figure 8 and Figure 13b, the

Mg and O strongly tend to form an amorphous phase and are restricted to 20 nm across the interface similar to how described by [37]. Figure 8 and Figure 13b also show that the Al and Fe elements have not inter-crossed beyond the 45 nm reaction zone. Furthermore, Al, Fe, and Si in the reaction zone are more likely to form the Al-Fe-Si phase at the nanoscale above the amorphous Mg- and O-rich layer [37]. The addition of Cr, however, changes the threshold of Al-Fe-Si phase formation [37], and a detailed study should be performed to quantify its effect, which is beyond the scope of this article. Similar elemental distributions of alloying elements were found throughout the interface without significant variation in the atomic %, implying a uniform and robustly bonded interface.

3.3 Joint strength and failure characteristics

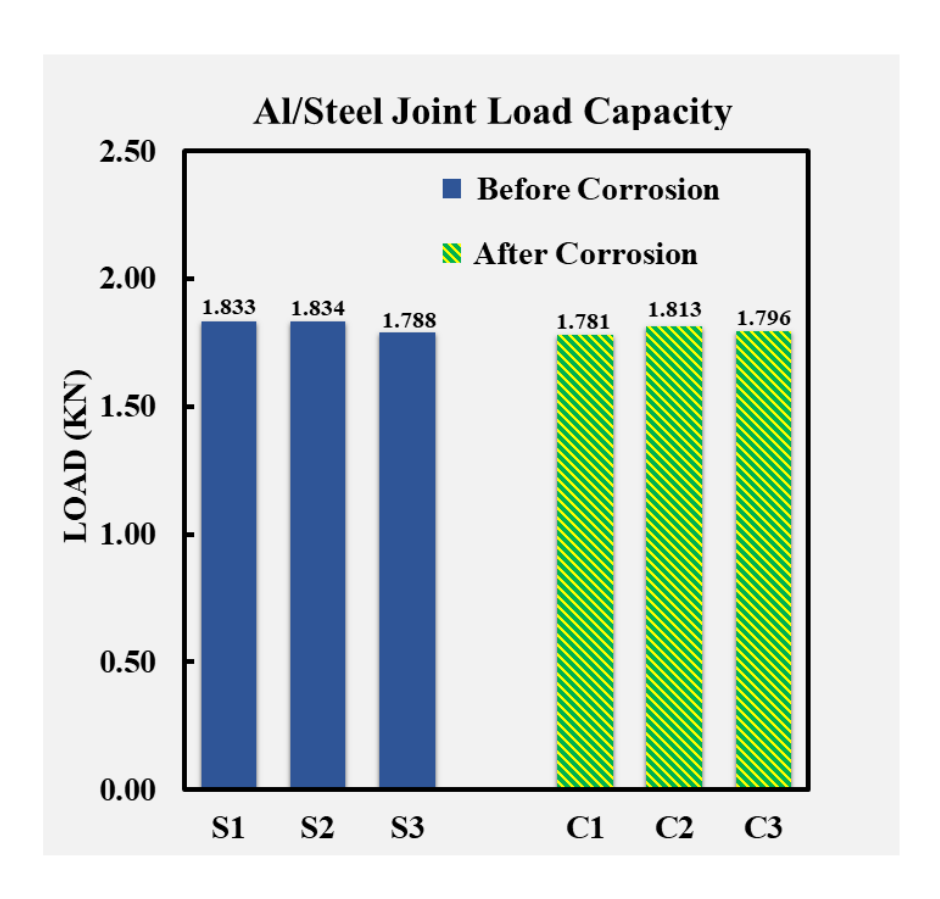


Figure 9: Al/Fe joint load capacity during lap shear tensile loading before and after corrosion conditions

As shown in Figure 9, the load capacity of the joint samples without being subjected to the corrosion cycles is at a minimum of 1.788 kN and a maximum of 1.833 kN, averaging at 1.818 kN with standard deviation of 0.026 kN among three specimens. In comparison, the load capacity of the joints after experiencing the corrosion cycles is at a minimum of 1.781 kN and a maximum of 1.813 kN, averaging at 1.797 kN with standard deviation of 0.016 kN. As can be seen, there is no significant difference between the average values of the joint load capacity before and after the corrosion cycles. It should be pointed out that maximum loads at failure (for with and without being subjected to corrosion cycle case) not the joint strengths are compared to determine the maximum load capacity of the joints. For deriving joint strength in terms of stress or joint strength at failure for comparing with other specimen types (e.g., Coach peel [40]) or structural applications, the mesh-insensitive structural stress methods [40–43] can be used, which is beyond the scope of this study.

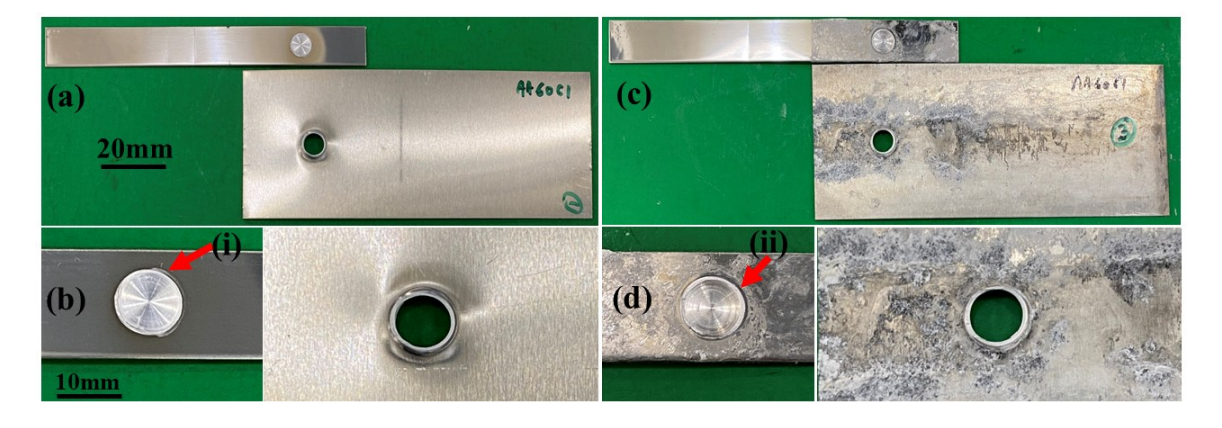


Figure 10: Failure features after lap shear tensile experiments, (a) & (b) global and local views before corrosion, and (c) & (d) global and local views after corrosion

Figure 10 shows the post-fracture images of the specimens after the lap shear tension testing. As shown in Figure 10b and 10d, the whole nugget of the spot joint was pulled away from the aluminum sheet and remained attached to the steel sheet post-tensile, often referred to as "pull

button" failure mode [44,45], regardless with or without being subjected to the corrosion cycles. It suggests that the corrosion cycle did not have any noticeable detrimental effects on the Al/Fe bond integrity. This is further confirmed by lap shear tension test results shown in Figure 9 which shows no noticeable deterioration of joint load capacity after corrosion cycles. It should be noted that such a "pull-button" mode (Figure 10) serves as an indication of a sufficient weld nugget strength and bond quality required ensuring adequate static and fatigue load capacity for structural applications [46].

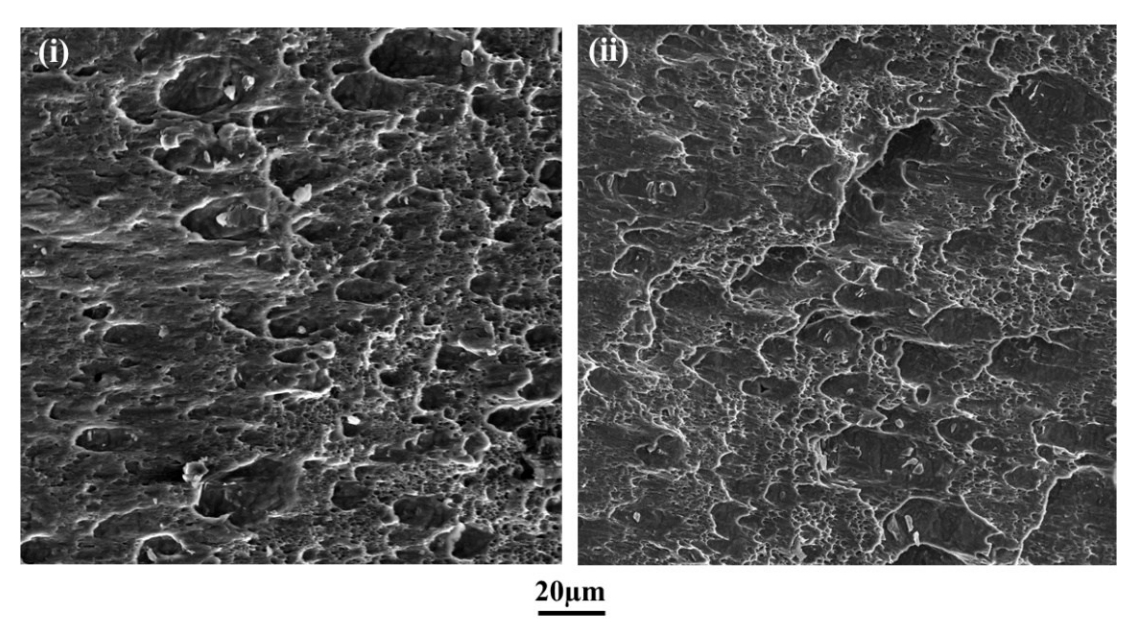


Figure 11: SEM micrographs at locations (i) and (ii) near the aluminum nugget shown in Figure 10, respectively.

As shown in Figure 11, fracture surface morphologies around the weld nugget boundary are consistently ductile for both cases with and without experiencing the corrosion cycles. A closer look at the fracture surface around the aluminum button remaining on the steel sheet in Figure 10b, shows significantly elongated dimples in Figure 11(i) for the case without experiencing corrosion cycles. Similar fracture surface features are also shown for the case subjected to the corrosion cycles, as shown in Figure 11(ii). These elongated dimple features signify the ductile fracture of

the aluminum nugget implying that all these specimens did not exhibit any brittle fracture either due to the presence of IMCs at the Al/Fe joint interface and/or any detrimental effects of corrosion-induced damage.

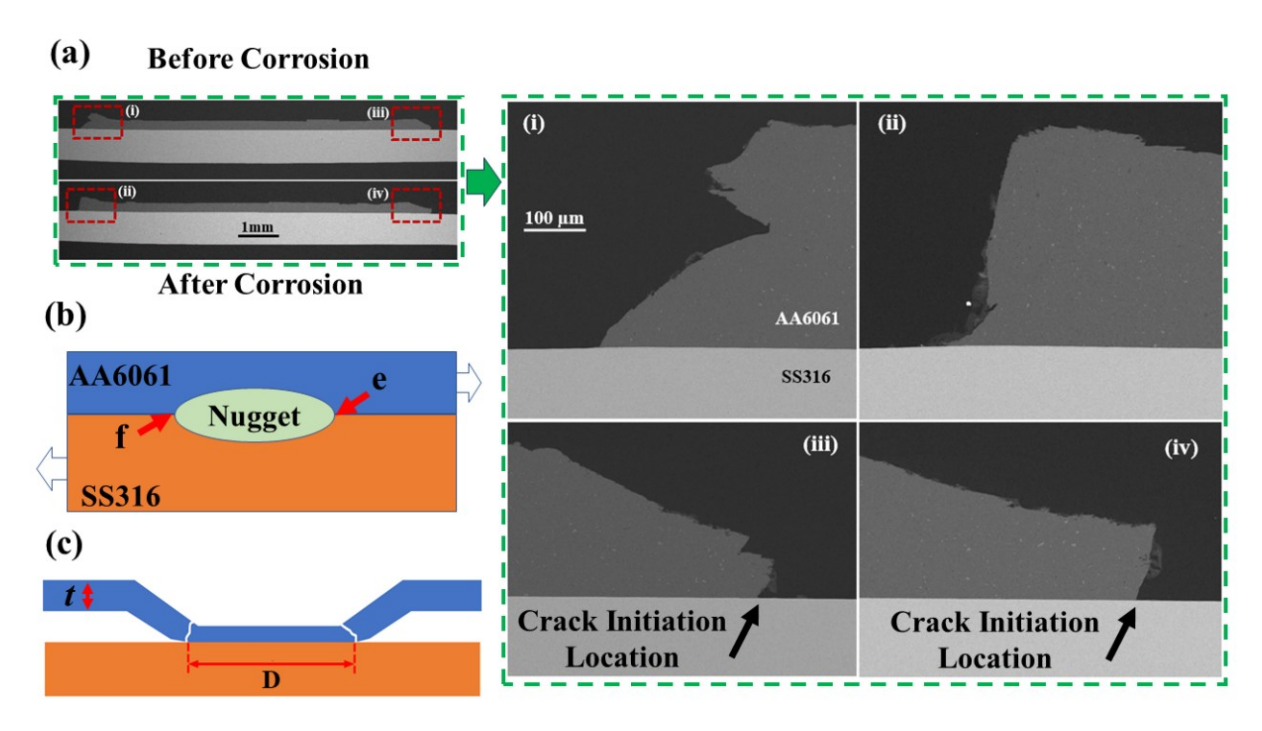


Figure 12: Fracture morphologies around the button failure at the nugget boundary, (a) global views, (b) schematic of nugget, (c) failure locations and failure paths during lap shear tensile experiments, (i-iv) detailed views of the locations i-iv shown in (a)

To investigate fracture development processes, Figure 12a shows the post-fracture weld cross-section images with detailed fracture path features (i) and (ii) (corresponding to location "d" in Figure 12b) and detailed features (iii) and (iv) (corresponding to location "c" in Figure 12b). In both cases (with and without experiencing corrosion cycles), the high-resolution images on the right side of Figure 12a show no evidence of damage or cracking at the Al/Fe interfacial notch tip. Both fracture initiation sites and final failure paths share a great resemblance between without and with corrosion cycling effects. The resulting failure mode is depicted in **Error! Reference source not found.**12c with or without considering corrosion cycles. In fact, it has been shown by a rigorous fracture mechanics analysis [9,41] that as long as $D/t \ge 3$, the "pull button" failure mode

becomes dominant, where D is the bonded nugget diameter shown in Figure 12c. In the present study, such a condition is obviously satisfied, as shown in Figure 12a.

4. Discussions

4.1 Suppression of IMCs

Development of IMCs at the Al/Fe interface is highly dependent on the diffusion constants of material, which in turn is governed by the interfacial temperature [14,47], relative mobility of the atoms, rate of material deformation, and cooling rate [28]. Liu et al. [48], Tanaka et al. [27], Beygi et al. [49], and Kimapong et al. [26] have shown that developing IMCs at the Al/Fe interface highly depends on the steel tool probe placement near the steel faying surface when joining aluminum alloy and steel plates. They have further found that the IMCs developed in two separate growth categories, one right where the tool probe was inserted in the steel material and the other under the shoulder where temperature distribution was found to be slightly higher than under the tool probe. Watanabe et al. [28] have systematically discussed the growth manner of the IMCs under various joining parameters and have suggested that keeping the stirring probe away from the steel-faying surface and restricting the joining temperature below the solidus temperature of the aluminum alloy favors the suppression of IMCs. Liu et al. [37] further conformed with the above observations and have achieved a novel form of amorphous phase while joining aluminum alloy to stainless steel under modified friction stir additive manufacturing. Derived by these principles, we have restricted the tool probe above the steel faying surface in spot joining configuration to provide a high shear strain rate and controlled temperature at the joining interface.

Under static diffusion bonding conditions, the inter-diffusion of elements is mainly governed by the diffusion coefficient [28]. The diffusion coefficient of aluminum into iron matrix

is zero up to 800 °C and diffusion coefficient of iron into aluminum matrix is zero up to 400°C, and above 400°C, the diffusion coefficient of Fe into Al increases significantly [28]. The interfacial temperature measurement at the boundary of the tooltip in our study showed that the maximum temperature was below 406°C throughout the joining process, suggesting the diffusion coefficient of Fe into Al must remain very small at the reaction zone. Beygi et al. [49] have recently presented a comparative study between carbon steel and stainless steel joining with aluminum alloy under friction stir welding conditions and showed the significance of alloying elements on the IMCs formation. They have observed that the presence of Cr can lower the IMCs thickness under material stirring conditions. On the other hand, Liu et al. [37] have shown that during the friction lap joining of aluminum alloy and stainless steel, the dominant mechanism for forming the joining interface was high shear strain rate driven nanoscale pre-melting that occurs much below the solidus to liquidus phase transition temperature (652 °C) [39]. Combined with the low cooling and extremely high strain rates, the T-T-T phase profile for such a process avoids the crystallization nose and provides an amorphous phase [39].

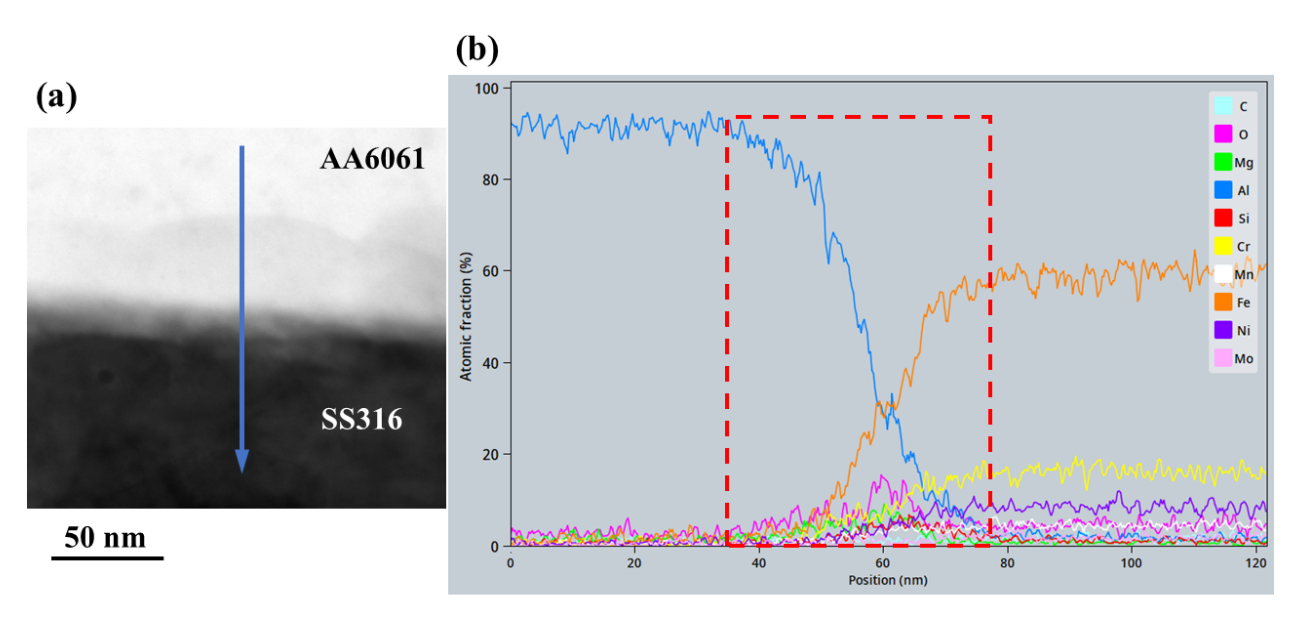


Figure 13: (a) EDS line analysis location across Al/Fe interface, and (b) elemental distribution across Al/Fe joint interface

Figure 13a shows a HAADF image with a blue arrow drawn running from the center of the image from top to the bottom direction. Figure 13b displays element profile curves collected along the arrow line and direction in Figure 13a. It can be seen that the reaction zone is 40-50 nm thick, conforming with the findings by Liu et al. [37]. The shear strain rate near the tooltip is $\sim 10^9 \, \text{s}^{-1}$, reasonably above the minimum required condition for a high shear strain rate stated by Liu et al. [37]. Based on the rationales presented by Liu et al. [37], such a reaction zone must contain ordered short-range structures that cannot be defined as IMCs (IMCs are dominantly in the form of crystalline structures) and must be in the form of an amorphous phase with some degree of nanocrystalline precipitates.

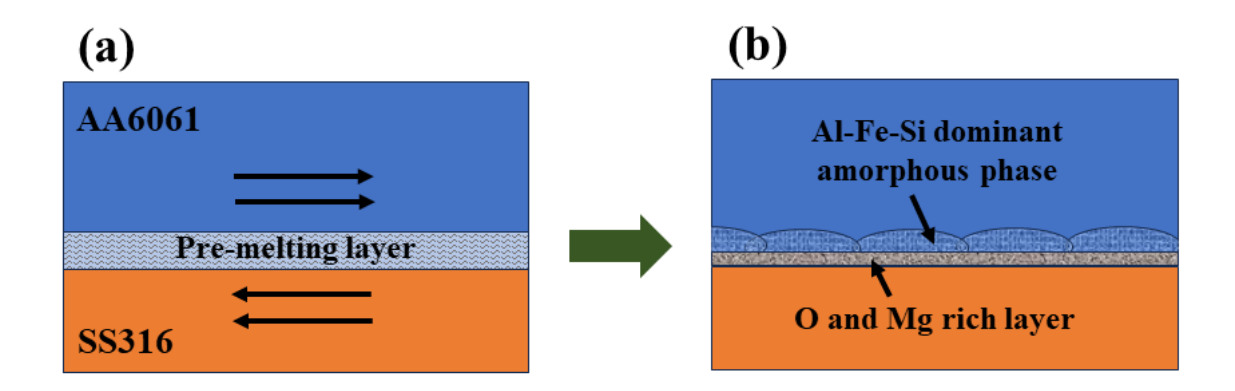


Figure 14: Schematic representation of the amorphous phase formation at the aluminum to steel joining interface produced via friction stir spot joining: (a) pre-melting layer formation due to intense friction induced high shear strain rate above the steel faying surface, and (b) amorphous phase formation as a graded reaction zone (or reaction layer) due to rapid quenching effect.

Liu et al. [37] have provided an in-depth discussion about the mechanisms associated with the formation of an amorphous phase at the 6061 aluminum alloy and 304 stainless steel interface, which involves a rapid shear localization induced pre-melting and suppression of atomic diffusion process as a result of a high shear strain rate in the order of 10⁹ s⁻¹. The present process follows the same principle, except that the aluminum alloy and stainless substrates are much thinner, i.e., 0.60

mm and 0.75 mm, respectively. The thin thickness combination studied here can be particularly challenging in maintaining a threshold nominal strain rate at the interface without causing any direct physical contact between the rotational tool face and the stainless substrate. As a result, the offset "h" in Figure 1 needs at the maximum value possible while still generating a relatively uniform shear strain rate at the interface. From the interface TEM characterization results shown in Figure 7, it can be seen that a consistent interfacial bond quality is evident without noticeable signs of IMCs, proving the robustness of the shear localization amorphization formation process presented by Liu et al. [37], even for thin gage aluminum-steel direct joining.

Liu et al. [37] have further demonstrated that the Al-Fe-Si rich phase developed as a qglass due to the cooling rate achieved by the friction stir additive manufacturing and the Mg and O rich layer developed as an amorphous-crystalline nano-composite. In the current study, the bulk volume is different, and the spot joining process time is relatively shorter than the one used by Liu et al. [37]. Furthermore, the heat dissipation time between the peak temperature and a characteristic temperature of 300 C achieved in the current study is approximately 3 seconds compared to the time obtained in similar processes by Liu et al. [50,51] are approximately above 5 seconds. Thus, it is understandable that the formed amorphous phase and its chemistry are different from the literature [37,49]. The formation mechanism of the amorphous phase can be explained in two steps, as shown in Figure 14. Firstly, a pre-melting liquid forms the interface between aluminum alloy 6061 and the stainless steel 316 faying surface (see Figure 14a) due to an intense frictional heating and high shear strain rate 109 s-1, similar to Liu et al. [37]. Differently, a faster cooling rate was achieved in the spot joining process configuration in the present study. It did not give sufficient time for diffused elements in the pre-melting layer to cluster themselves once the shear strain rate is removed. Secondly, the amorphous phase is then formed with a much high chemical homogeneity after the shear strain has been released (see Figure 14b) due to a high cooling rate achieved along with a much smaller bulk material used here compared to those used in Liu et al. [37,38]. A more sophisticated analytical and experimental analysis is necessary to further elucidate the interface microstructure formation mechanism which is beyond the scope of this article.

4.2 Corrosion effects

As stated in the introduction section, IMCs are detrimental to dissimilar material joints as due to their brittle nature which can trigger premature failure under load [52]. IMCs can also form galvanic cells at the Al/Fe joint interface [29]. Wloka et al. [29] reported that Fe-containing IMCs at the joining zone acted as cathode and reduced the open circuit potential (OCP). Next to the IMCs, the corrosion was found to be faster to dissolve the Al-IMC interface. Thus, the joining zone between aluminum alloy and galvanized steel had the most negative corrosion potential and was the first to corrode. Zhang et al. [17] have also shown that the OCP difference between IMCs and aluminum becomes the largest under corrosive conditions, leading to accelerated corrosion of the Al-IMCs interface and weakening the joining interface significantly. Sravanthi et al. [32] have shown that an increased amount of IMCs at the joint interface between aluminum alloy and mild steel was mainly responsible for localized corrosion at the joint interface. They also found that the increased thickness of IMCs at the joint interface further increased the base material grain boundary widths and weakened the joint interface further.

As it has been well established that IMCs are crystalline solids with well-defined grain boundaries which are highly susceptible to corrosion [53]. Bennett et al. [54] have shown that sensitization in stainless steel was found to be exacerbated by the grain boundaries leading to rapid corrosion at the grain boundaries and intergranular corrosion. For aluminum-based alloys, a sequential pitting initiation, pitting propagation and the intergranular corrosion were found to be

accelerated by the depletion of noble Si near the grain boundaries [55]. Hoffman et al. [56] further elucidated that the CoCrMo alloys show preferential grain boundary attacks around high-energy grain boundaries as a consequence of grain boundary sensitization. They further showed that the grain boundaries were mainly responsible for the crevice and intergranular corrosion due to the penetration of the electrolytic ions. In contrast, amorphous phase does not contain any ordered structure or grain boundaries and offers a high degree of resistance to corrosive media [57]. Naka et al. [58] showed that the corrosion resistance of amorphous copper-based alloy was higher than that of crystalline alloys with the same composition. They further confirmed that the chemical homogeneity increments due to the glass formation increased the corrosion resistance in the amorphous metal-metal system. Bakare et al. [59] have shown that the crystalline form of an ironbased alloy showed preferential dissolution of Mo-rich precipitates and shown accelerated corrosion compared to the amorphous form of the alloy with the same composition. They further attributed the improved corrosion resistance of the amorphous material to the chemical homogeneity and resistance of the amorphous phase for electrolytic ions. Based on the above documented findings in the literature, this study further confirms that the amorphous phase formed at the aluminum alloy 6061 and stainless steel 316 indeed serves as an effective barrier for corrosion attacks, at least under the automotive grade corrosion cycles.

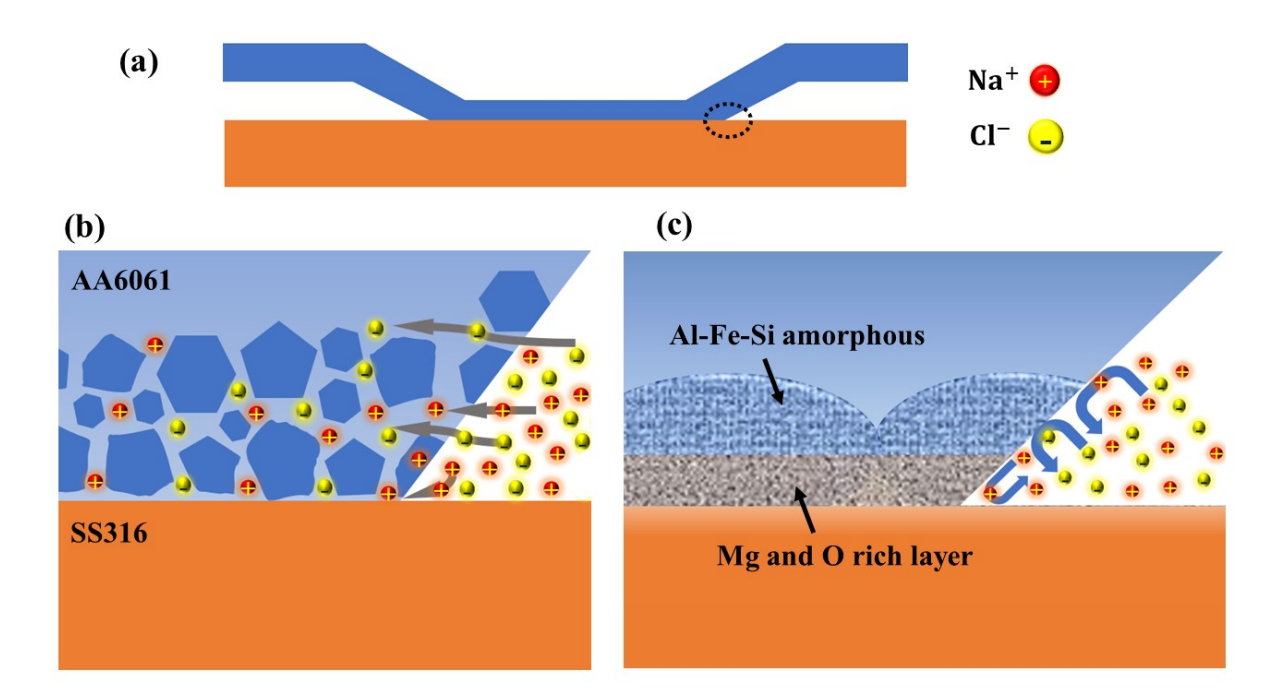


Figure 15: Schematic illustration of corrosion resistance via amorphous reaction zone at the aluminum/steel joining interface achieved via NSSLIA: (a) schematic representing spot joining configuration, (b) representation of corrosive media electrolytic ions penetration through grain boundaries of crystalline grain boundaries in IMCs, and (c) barrier effect to prevent the penetration of corrosive media electrolytic ions via the amorphous phase reaction zone

Based on the discussions above and the experimental characterizations performed in this study, the corrosion-resistant nature of the amorphous interfacial layer can be postulated as shown in Figure 15 above. It should be noted here that the grain boundaries are exaggerated to schematically depict the electrolytic ion transfer from the corrosive media towards the Al/Steel interface in Figure 15b. Since the grain boundaries are the regions of atomic packing discontinuity, the diffusion of ions from the electrolytic media gets accelerated through the grain boundaries. It reaches the steel surface through the crystalline IMCs, easily allowing the preferential grain boundary corrosion attack. Additionally, the potential difference between a single grain and the grain boundaries is always present due to the difference in microstructure homogeneity (due to the presence of defects, slip, and dislocations). The micro-galvanic cell formation is accelerated around the crystalline solids such as IMCs, and ion exchange becomes faster to corrode the joining

interface. On the other hand, the amorphous dominant reaction zone (Figure 15c) acts as a barrier to prevent the ion exchange between the bulk electrolytic corrosive media and the joining interface due to its chemical homogeneity. Such a barrier effect does not allow for a preferential corrosion attack or micro-galvanic cell formation around the joining interface, increasing the corrosion resistance of the joints.

Furthermore, as described in Section 3, all Al/Steel spot joint samples, with and without being subjected to the corrosion cycles, have consistently exhibited ductile failure mode (see Figure 11 and Figure 12) in the form of "pull button", as illustrated in Error! Reference source not found.12c. There is also a noticeable amount of thinning around the notch near the joining nugget boundaries due to the plunging action of the friction stir tool. This thinning can be observed with a continuous profile from the actual sheet thickness down to the joining sheet thickness in the nugget area (Figures 5 and 12). However, the amount of thinning is nearly the same in both with and without being subjected to the corrosion cycle cases and has been found not to alter the failure modes in both conditions. The resulting relatively consistent joint strengths in terms of test specimen load capacities shown in Figure 9 further proves the corrosion-resistant nature of the spot joints realized by shear localization based direct joining method presented in this study.

5. Conclusions

A shear localization-based spot welding method is presented for joining thin gauge aluminum alloy to stainless steel sheets with a consistent bond quality with negligible detrimental intermetallic compounds, if any. Environmental corrosion effects on joint strengths were examined by subjecting a batch of aluminum alloy (6061-T6) and stainless steel (316) joint samples to a

well-accepted corrosion environment conditions by the automotive industry. The following represent the key findings:

- i. The nanoscale shear localization induced alloy amorphization (NSLIAA) discovered by Liu et al. [37] can be consistently reproduced for direct spot-joining of thin aluminum alloy (AA6061-T6) to thin stainless steel (SS316) substrates without noticeable IMCs. This further proves the robustness of the NSLIAA process for potentially a broad application in the direct joining of incompatible metals.
- ii. A continuous amorphous dominant reaction zone was observed at the bimetallic joining interface, consisting of an Mg and O-rich layer adjacent to the steel faying surface in combination with an Al-Fe-Si amorphous phase. The continuous reaction zone was attributed to the faster cooling rate effect observed for the spot joining configuration and high shear strain rate dominant material pre-melting at the joining interface.
- iii. The resulting bimetallic spot joints show no degradation in joint strengths, nor any change in failure mode after being subjected to a full automotive grade corrosion test cycle. The continuous and homogeneous amorphous reaction zone did not allow the electrolytic ion penetration at the joining interface and was found to have a barrier effect under the automotive corrosion cycling conditions.
- iv. The good corrosion resistance thus observed in the Al/Steel joints investigated in this study can be attributed to the amorphous phase at the joining interface. The results suggest that the NSLIAA process has a strong potential for enabling direct joining between incompatible metals to achieve structural lightweighting for applications in severe and harsh environmental conditions.

Acknowledgements:

This work was supported by the National Science Foundation grant (NSF CMMI 2126163), and the authors acknowledge the technical support from the Michigan Center for Materials Characterization (MC2). They also acknowledge Ben Houle's support for preparing the temperature measurement setup.

References:

- [1] Skszek T, Conklin J. Multi-Material Lightweight Vehicles Acknowledgement 2014.
- [2] Kleinbaum S, Jiang C, Logan S. Enabling sustainable transportation through joining of dissimilar lightweight materials. MRS Bull 2019;44:608–12. https://doi.org/DOI: 10.1557/mrs.2019.178.
- [3] Pereira JAC, Kasaei MM, Carbas RJC, Marques EAS, Lim H, da Silva LFM. Joining magnesium and aluminum alloy sheets by a novel hole hemming process. Thin-Walled Struct 2023;187:110758. https://doi.org/10.1016/j.tws.2023.110758.
- [4] Gullino A, Matteis P, Aiuto FD. Review of aluminum-to-steel welding technologies for car-body applications. Metals (Basel) 2019;9:1–28. https://doi.org/10.3390/met9030315.
- [5] Czerwinski F. Current trends in automotive lightweighting strategies and materials.

 Materials (Basel) 2021;14. https://doi.org/10.3390/ma14216631.
- [6] Lam KP, Behdinan K, Cleghorn WL. A material and gauge thickness sensitivity analysis on the NVH and crashworthiness of automotive instrument panel support. Thin-Walled Struct 2003;41:1005–18. https://doi.org/10.1016/S0263-8231(03)00050-8.
- [7] Haran-Nogueira A, Kasaei MM, Akhavan-Safar A, Carbas RJC, Marques EAS, da Silva

- LFM. Failure analysis of hybrid bonded-hole hemmed joints for dissimilar materials. Thin-Walled Struct 2023;189:110907. https://doi.org/10.1016/j.tws.2023.110907.
- [8] Sadeghian A, Iqbal N. A review on dissimilar laser welding of steel-copper, steel-aluminum, aluminum-copper, and steel-nickel for electric vehicle battery manufacturing.

 Opt Laser Technol 2022;146:107595. https://doi.org/10.1016/j.optlastec.2021.107595.
- [9] Khan, A. S., Dong, P., Liu, F., Zhang Y. Directly Welding Plastic to Metal for Structural Applications: a state-of-the-art review Part I Promising Processes. Weld J 2023.
- [10] Derazkola HA, Simchi A. An investigation on the dissimilar friction stir welding of T-joints between AA5754 aluminum alloy and poly(methyl methacrylate). Thin-Walled Struct 2019;135:376–84. https://doi.org/10.1016/j.tws.2018.11.027.
- [11] Chen Y, Yang X, Li M, Wei K, Li S. Mechanical behavior and progressive failure analysis of riveted, bonded and hybrid joints with CFRP-aluminum dissimilar materials. Thin-Walled Struct 2019;139:271–80. https://doi.org/10.1016/j.tws.2019.03.007.
- [12] Zain-ul-Abidin, Khan SA, Khan HA, Awais R, Khushbash S. Classification of progressive failure and mechanical behavior of dissimilar material hybrid joints at varying temperatures. Thin-Walled Struct 2023;182:110212. https://doi.org/10.1016/j.tws.2022.110212.
- [13] Khan AS, Liu F, Dong P. Joining of metal and non-polar polypropylene composite through a simple functional group seeding layer. J Manuf Process 2023;85:90–100. https://doi.org/10.1016/j.jmapro.2022.11.022.
- [14] Pan B, Sun H, Shang SL, Banu M, Wang PC, Carlson BE, et al. Understanding formation

- mechanisms of intermetallic compounds in dissimilar Al/steel joint processed by resistance spot welding. J Manuf Process 2022;83:212–22. https://doi.org/10.1016/j.jmapro.2022.08.062.
- [15] Shi L, Kang J, Chen X, Haselhuhn AS, Sigler DR, Carlson BE. Effect of material inhomogeneity on fracture modes in aluminium–steel resistance spot welds. Fatigue Fract Eng Mater Struct 2020;43:2157–68. https://doi.org/10.1111/ffe.13256.
- [16] Atabaki MM, Nikodinovski M, Chenier P, Ma J, Harooni M, Kovacevic R. Welding of Aluminum Alloys to Steels: An Overview. J Manuf Sci Prod 2014;14:59–78. https://doi.org/10.1515/jmsp-2014-0007.
- [17] Zhang S, Li S, Meng X, Chen Y, Cheng C. Effect of intermetallic compound on the corrosion behaviour of resistance spot welding joints between 5182 aluminium alloy and galvanized DP780 dual-phase steel. Mater Res Express 2023;10. https://doi.org/10.1088/2053-1591/acbbbc.
- [18] Fereiduni E, Movahedi M, Kokabi AH. Aluminum/steel joints made by an alternative friction stir spot welding process. J Mater Process Technol 2015;224:1–10. https://doi.org/10.1016/j.jmatprotec.2015.04.028.
- [19] Hussein SA, Tahir ASM, Hadzley AB. Characteristics of aluminum-to-steel joint made by friction stir welding: A review. Mater Today Commun 2015;5:32–49. https://doi.org/10.1016/j.mtcomm.2015.09.004.
- [20] Zhao H, Liu Y, Ma Y, Ping X, Zhang D. Thin-Walled Structures Research on the formation mechanism and mechanical properties of refill friction stir riveting (RFSR) joints of aluminium alloy AA7075-T6. Thin-Walled Struct 2024;198:111696.

- https://doi.org/10.1016/j.tws.2024.111696.
- [21] Akramifard HR, Mirzadeh H, Parsa MH. Cladding of aluminum on AISI 304L stainless steel by cold roll bonding: Mechanism, microstructure, and mechanical properties. Mater Sci Eng A 2014;613:232–9. https://doi.org/10.1016/j.msea.2014.06.109.
- [22] Aizawa T, Kashani M, Okagawa K. Application of magnetic pulse welding for aluminum alloys and SPCC steel sheet joints. Weld J (Miami, Fla) 2007;86:119–24.
- [23] Chen S, Daehn GS, Vivek A, Liu B, Hansen SR, Huang J, et al. Interfacial microstructures and mechanical property of vaporizing foil actuator welding of aluminum alloy to steel.

 Mater Sci Eng A 2016;659:12–21. https://doi.org/10.1016/j.msea.2016.02.040.
- [24] Vivek A, Hansen SR, Liu BC, Daehn GS. Vaporizing foil actuator: A tool for collision welding. J Mater Process Technol 2013;213:2304–11. https://doi.org/10.1016/j.jmatprotec.2013.07.006.
- [25] Ma H, Qin G, Geng P, Ao Z, Chen Y. Effect of intermetallic compounds on the mechanical property and corrosion behaviour of aluminium alloy/steel hybrid fusionbrazed welded structure. J Manuf Process 2022;75:170–80. https://doi.org/10.1016/j.jmapro.2022.01.004.
- [26] Kimapong K, Watanabe T. Friction stir welding of aluminum alloy to steel. Weld J (Miami, Fla) 2004;83:277–82.
- [27] Tanaka T, Nezu M, Uchida S, Hirata T. Mechanism of intermetallic compound formation during the dissimilar friction stir welding of aluminum and steel. J Mater Sci 2020;55:3064–72. https://doi.org/10.1007/s10853-019-04106-2.

- [28] Watanabe M, Feng K, Nakamura Y, Kumai S. Growth manner of intermetallic compound layer produced at welding interface of friction stir spot welded aluminum/steel lap joint.

 Mater Trans 2011;52:953–9. https://doi.org/10.2320/matertrans.L-MZ201120.
- [29] Wloka J, Laukant H, Glatzel U, Virtanen S. Corrosion properties of laser beam joints of aluminium with zinc-coated steel. Corros Sci 2007;49:4243–58. https://doi.org/10.1016/j.corsci.2007.04.014.
- [30] Xia H, Zhao X, Tan C, Chen B, Song X, Li L. Effect of Si content on the interfacial reactions in laser welded-brazed Al/steel dissimilar butted joint. J Mater Process Technol 2018;258:9–21. https://doi.org/10.1016/j.jmatprotec.2018.03.010.
- [31] Shi Y, Li J, Zhang G, Huang J, Gu Y. Corrosion Behavior of Aluminum-Steel Weld-Brazing Joint. J Mater Eng Perform 2016;25:1916–23. https://doi.org/10.1007/s11665-016-2020-9.
- [32] Sravanthi SS, Acharyya SG, Phani Prabhakar K V., Padmanabham G. Effect of Welding Parameters on the Corrosion Behavior of Dissimilar Alloy Welds of T6 AA6061 Al-Galvanized Mild Steel. J Mater Eng Perform 2018;27:5518–31. https://doi.org/10.1007/s11665-018-3596-z.
- [33] Ma H, Qin G, Geng P, Wang S, Zhang D. Microstructural characterisation and corrosion behaviour of aluminium alloy/steel hybrid structure produced by friction welding. J Manuf Process 2021;61:349–56. https://doi.org/10.1016/j.jmapro.2020.11.014.
- [34] Watanabe T, Takayama H, Yanagisawa A. Joining of aluminum alloy to steel by friction stir welding. J Mater Process Technol 2006;178:342–9. https://doi.org/10.1016/j.jmatprotec.2006.04.117.

- [35] Beygi R, Zarezadeh Mehrizi M, Akhavan-Safar A, Safaei S, Loureiro A, da Silva LFM.

 Design of friction stir welding for butt joining of aluminum to steel of dissimilar thickness: heat treatment and fracture behavior. Int J Adv Manuf Technol 2021;112:1951–64. https://doi.org/10.1007/s00170-020-06406-3.
- [36] Beygi R, Carbas RJC, Barbosa AQ, Marques EAS, da Silva LFM. Buttering for FSW: Enhancing the fracture toughness of Al-Fe intermetallics through nanocrystallinity and suppressing their growth. J Manuf Process 2023;90:233–41. https://doi.org/10.1016/j.jmapro.2023.02.001.
- [37] Liu FC, Dong P, Khan AS, Sun K, Lu W, Taub A, et al. Amorphous interfacial microstructure and high bonding strength in Al-Fe bimetallic components enabled by a large-area solid-state additive manufacturing technique. J Mater Process Technol 2022;308. https://doi.org/10.1016/j.jmatprotec.2022.117721.
- [38] Zhang M, Liu FC, Liu ZY, Xue P, Dong P, Zhang H, et al. Highly stable nanoscale amorphous microstructure at steel-aluminum interface enabled by a new solid-state additive manufacturing method. Scr Mater 2023;227. https://doi.org/10.1016/j.scriptamat.2023.115300.
- [39] Liu F, Zhang Y, Dong P. Large area friction stir additive manufacturing of intermetallic-free aluminum-steel bimetallic components through interfacial amorphization. J Manuf Process 2022;73:725–35. https://doi.org/10.1016/j.jmapro.2021.11.042.
- [40] KHAN AS, DONG P, LIU F, ZHANG Y. A State-of-the-Art Review on Direct Welding of Polymer to Metal for Structural Applications: Part 2 — Joint Design and Property Characterization. Weld J 2024;103:142–50. https://doi.org/10.29391/2024.103.013.

- [41] Zhang Y, Dong P, Pei X. Fracture Mechanics Modeling of Fatigue Behaviors of Adhesive-Bonded Aluminum Alloy Components. Metals (Basel) 2022;12. https://doi.org/10.3390/met12081298.
- [42] Lu H, Dong P, Boppudi S. Strength analysis of fillet welds under longitudinal and transverse shear conditions. Mar Struct 2015;43:87–106. https://doi.org/10.1016/j.marstruc.2015.06.003.
- [43] Kang HT, Dong P, Hong JK. Fatigue analysis of spot welds using a mesh-insensitive structural stress approach. Int J Fatigue 2007;29:1546–53. https://doi.org/10.1016/j.ijfatigue.2006.10.025.
- [44] Sun X, Stephens E V., Khaleel MA. Effects of fusion zone size and failure mode on peak load and energy absorption of advanced high-strength steel spot welds. Weld J (Miami, Fla) 2007;86.
- [45] Martinsen K, Hu SJ, Carlson BE. Joining of dissimilar materials. CIRP Ann Manuf Technol 2015;64:679–99. https://doi.org/10.1016/j.cirp.2015.05.006.
- [46] Zhang L, Dong P, Wang Y, Mei J. A Coarse-Mesh hybrid structural stress method for fatigue evaluation of Spot-Welded structures. Int J Fatigue 2022;164:107109. https://doi.org/https://doi.org/10.1016/j.ijfatigue.2022.107109.
- [47] Luo Y, Hu SP, Song XG, Aprilia A, Yang YJ, Zhou W. A novel method for improving interfacial joining strength of vacuum brazed TiAl/GH3536 thin-walled structure by Au coating. Thin-Walled Struct 2023;190. https://doi.org/10.1016/j.tws.2023.110915.
- [48] Liu FC, Dong P. From thick intermetallic to nanoscale amorphous phase at Al-Fe joint

- interface: roles of friction stir welding conditions. Scr Mater 2021;191:167–72. https://doi.org/10.1016/j.scriptamat.2020.09.031.
- [49] Beygi R, Carbas R, Queiros A, Marques EAS, Shi R, da Silva LFM. Comparative Study Between Stainless Steel and Carbon Steel During Dissimilar Friction Stir Welding with Aluminum: Kinetics of Al–Fe Intermetallic Growth. Met Mater Int 2022;28:1948–59. https://doi.org/10.1007/s12540-021-01070-y.
- [50] Liu F, Dong P, Khan AS, Zhang Y, Cheng R, Taub A, et al. 3D printing of fine-grained aluminum alloys through extrusion-based additive manufacturing: Microstructure and property characterization. J Mater Sci Technol 2023;139:126–36.

 https://doi.org/10.1016/j.jmst.2022.08.017.
- [51] Zhang M, Liu FC, Xue P, Zhang H, Wu LH, Ni DR, et al. Fabrication of large-scale steel-aluminum components with homogenously distributed amorphous interfacial layer and enhanced bonding strength using modified friction stir additive manufacturing. J Mater Sci Technol 2024;194:151–66. https://doi.org/10.1016/j.jmst.2024.01.036.
- [52] Song JL, Lin SB, Yang CL, Ma GC, Liu H. Spreading behavior and microstructure characteristics of dissimilar metals TIG welding-brazing of aluminum alloy to stainless steel. Mater Sci Eng A 2009;509:31–40. https://doi.org/10.1016/j.msea.2009.02.036.
- [53] Paul AR, Mukherjee M, Singh D. A Critical Review on the Properties of Intermetallic Compounds and Their Application in the Modern Manufacturing. Cryst Res Technol 2022;57:1–19. https://doi.org/10.1002/crat.202100159.
- [54] Bennett BW, Pickering HW. Effect of grain boundary structure on sensitization and corrosion of stainless steel. Metall Trans A 1991;18:1117–24.

- https://doi.org/10.1007/BF03325722.
- [55] Shi A, Shaw BA, Sikora E. The role of grain boundary regions in the localized corrosion of a copper-free 6111-like aluminum alloy. Corrosion 2005;61:534–47. https://doi.org/10.5006/1.3278189.
- [56] Hoffman EE, Lin A, Liao Y, Marks LD. Grain boundary assisted crevice corrosion in CoCrMo alloys. Corrosion 2016;72:1445–61. https://doi.org/10.5006/2108.
- [57] Botta WJ, Berger JE, Kiminami CS, Roche V, Nogueira RP, Bolfarini C. Corrosion resistance of Fe-based amorphous alloys. J Alloys Compd 2014;586:S105–10. https://doi.org/10.1016/j.jallcom.2012.12.130.
- [58] Naka M, Hashimoto K, Masumoto T. Corrosion behavior of amorphous and crystalline Cu50Ti50 and Cu50Zr50 alloys. J Non Cryst Solids 1978;30:29–36. https://doi.org/10.1016/0022-3093(78)90053-4.
- [59] Bakare MS, Voisey KT, Chokethawai K, Mccartney DG. Corrosion Behaviour of Crystalline and Amorphous Forms of the n.d.